nanomaterials

MDPI

Article

Carbon Nanotube-Modified Nickel Hydroxide as Cathode Materials for High-Performance Li-S Batteries

Qianwen Jin [1], Yajing Yan [1], Chenchen Hu [1], Yongguang Zhang [1,*], Xi Wang [2,*] and Chunyong Liang [1,*]

[1] State Key Laboratory of Reliability and Intelligence of Electrical Equipment, School of Materials Science and Engineering, Hebei University of Technology, Tianjin 300130, China; jinqianwen111@163.com (Q.J.); yajingy@126.com (Y.Y.); h15364966537@163.com (C.H.)
[2] China Center for Information Industry Development, Beijing 100048, China
* Correspondence: yongguangzhang@hebut.edu.cn (Y.Z.); wangxi@ccidthinktank.com (X.W.); liangchunyong@hebut.edu.cn (C.L.)

Abstract: The advantages of high energy density and low cost make lithium–sulfur batteries one of the most promising candidates for next-generation energy storage systems. However, the electrical insulativity of sulfur and the serious shuttle effect of lithium polysulfides (LiPSs) still impedes its further development. In this regard, a uniform hollow mesoporous $Ni(OH)_2$@CNT microsphere was developed to address these issues. The SEM images show the $Ni(OH)_2$ delivers an average size of about 5 μm, which is composed of nanosheets. The designed $Ni(OH)_2$@CNT contains transition metal cations and interlayer anions, featuring the unique 3D spheroidal flower structure, decent porosity, and large surface area, which is highly conducive to conversion systems and electrochemical energy storage. As a result, the as-fabricated Li-S battery delivers the reversible capacity of 652 mAh g^{-1} after 400 cycles, demonstrating excellent capacity retention with a low average capacity loss of only 0.081% per cycle at 1 C. This work has shown that the $Ni(OH)_2$@CNT sulfur host prepared by hydrothermal embraces delivers strong physical absorption as well as chemical affinity.

Keywords: Li-S battery; carbon nanotube; nickel hydroxide; cathode

Citation: Jin, Q.; Yan, Y.; Hu, C.; Zhang, Y.; Wang, X.; Liang, C. Carbon Nanotube-Modified Nickel Hydroxide as Cathode Materials for High-Performance Li-S Batteries. *Nanomaterials* **2022**, *12*, 886. https://doi.org/10.3390/nano12050886

Academic Editors: Emmanuel Iwuoha and Xuezhi Song

Received: 4 December 2021
Accepted: 26 February 2022
Published: 7 March 2022

1. Introduction

Lithium–ion batteries (LIBs), commercialized since the 1990s, have been leading the secondary battery market [1,2]. However, the development of LIBs is constrained by their limited theoretical energy density [3–5]. The booming Li-S battery has emerged as the most prospective battery due to its salient theoretical specific capacities of lithium and sulfur [6,7]. Elemental sulfur as a low-cost and non-toxic material, theoretically offers a high capacity of 1675 mAh g^{-1} [8,9]. Despite the numerous advantages, its commercialization path for lithium-sulfur batteries is still hindered by certain intrinsic factors [10–12]. First, sulfur and sulfides have poor electronic conductivity, resulting in low active materials utilization and specific capacity [13]. Second, a great structure and volume change (~80%) in the process of cycling causes hidden dangers for electrode structural stability [14]. Thirdly and most important, "shuttle effect" caused by the LiPSs dissolution causes poor cycle stability, which obstructs the practical application of Li-S batteries [15].

Considerable research work has been made to tackle the aforementioned challenges. Based on the natural intrinsic conductivity and a stable skeleton structure, various porous carbon materials such as carbon nanospheres [16], graphene [17], carbon nanotubes (CNTs) [18], and carbide-derived carbons have been developed as cathodes for high performance Li-S batteries. Unfortunately, albeit the considerable progress, the physical interaction between the nonpolar carbon and LiPSs is too weak for sufficient sulfur fixation [16]. In view of this, polar materials such as metal oxides (MOs), metal sulfides (MSs), and metal-organic frameworks (MOFs) [19] have been extensively studied for their ability to form strong chemical bonds with LiPSs. For example, TiO_2 [13], MnO_2 [7], Al_2O_3 [18],

ZnO [20], $Co(OH)_2$ [21], and ZrO_2 [22] showed excellent performance as sulfur host materials. As expected, both metal oxides and metal hydroxides as S host cathodes exhibit high discharge capacity and excellent cycling stability [23–26]. Compared with other metal (hydrogen) oxides, $Ni(OH)_2$ has become a promising material due to its low cost and strong chemical bonding with LiPS. Zhang et al. use $Ni(OH)_2$ nanoparticles as surface modifiers, a new type of $Ni(OH)_2$ surface-modified C/S composites was prepared [27]. This modifier acts to strengthen the LiPS adsorption performance and inhibiting the migration of S, so that excellent electrochemical performance can be achieved. Xu et al. develop a three-dimensional porous hollow structure of $Ni(OH)_2$ as the S host material [28], and the outer nanosheets endow it with large specific surface area and abundant active sites while acting as a conductive scaffold. Zhao et al. reported that rGO-coated $Ni(OH)_2$ materials encapsulated sulfur nanoparticles could significantly improve the specific capacity and long-term cycling stability of lithium-sulfur batteries [29]. The introduction of porous CNT as a support material for LiPSs, not only improves the 3D conductive network structure, but also facilitates the electron transportation, resulting in high-rate capabilities [30]. Therefore, it is very promising to design a composite that decorates carbon nanotubes on nickel hydroxide nanosheets [31,32]. It can combine the advantages and alleviate the disadvantages of the two components [33,34].

Herein, we designed the CNTs reinforced hollow mesoporous $Ni(OH)_2$ as a free-standing sulfur host matrix. In this structure, CNTs were grown on $Ni(OH)_2$ nanosheets and wrapped active sulfur nanoparticles as an effective carrier to enable confinement shuttle effect whilst promoting their reaction kinetics. In addition, S/$Ni(OH)_2$@CNT as the cathode for Li-S batteries, which have several apparent ad vantages. First, one-dimensional CNTs could provide fast electron transport paths [35], and hollow core acts as a nanoscale electrochemical reaction vessel that efficiently limits the large volume variation. Furthermore, the introduction of these abundant functional polar/hydrophilic groups of $Ni(OH)_2$ nanosphere could restrict the "shuttle effect" of LiPSs through strong chemical adsorption [36–40]. Meanwhile, the intermediate thiosulfate generated by the reaction of nickel hydroxide and LiPSs can accelerate the redox kinetics and promote cycle stability [41,42]. As a result, the Li-S batteries assembled by $Ni(OH)_2$@CNT cathode obtained excellent electrochemical performance, which opens up a new way for the research of cathode materials for Li-S batteries.

2. Experimental Section

2.1. Synthesis of $Ni(OH)_2$@CNT and S/$Ni(OH)_2$@CNT Composite

Materials: Ammonium hydroxide solution (28%, Aladdin, Shanghai, China), $NiCl_2 \cdot 6H_2O$ (99.9%, Aladdin, Shanghai, China), Urea (99.5%, Aladdin, Shanghai, China), Carbon nanotube dispersion (CNTs, 10 wt%, Aladdin, Shanghai, China).

Synthesis of $Ni(OH)_2$@CNT composite: Using deionized water as the solution, configure 15 mL 0.2 M anhydrous nickel chloride and 15 mL 2 M urea solution. The two solutions were mixed to form a light green solution, which was stirred at a rotation speed of 300 r/min for 30 min. Under the strong stirring of 600 r/min, 6 mL of 13% aqueous ammonia solution was dropped into the above solution dropwise to form a blue solution. Take 400 mg of carbon nanotube dispersion (~10 wt%) and disperse it in 30 mL of absolute ethanol. The two solutions were uniformly mixed and then transferred to an autoclave for reaction at 120 °C for 12 h. Transfer the reacted solution into centrifuge tube, wash with deionized water, and centrifuge three times to remove soluble impurities [8]. The centrifuged product was collected to obtain $Ni(OH)_2$@CNT.

Preparation of Sulfur-Based Composites: The S/$Ni(OH)_2$@CNT composites were prepared by a melt impregnation method. First, sublimated sulfur was thoroughly mixed with the as-prepared $Ni(OH)_2$@CNT at a mass ratio of 3:1, followed by heat treatment at 155 °C for 12 h under an inert atmosphere [43]. That is, S/$Ni(OH)_2$@CNT is obtained. According to the SEM image shown in Figure S1, sublimation S is fully mixed with $Ni(OH)_2$@CNT. Evenly distributed CNTs provide a guarantee for the electron transfer of the electrode. For

comparison, S/$Ni(OH)_2$ and S/CNT composites were prepared with $Ni(OH)_2$ and CNT as sulfur host, respectively.

2.2. Materials Characterization

The surface morphology of the samples was examined using scanning electron microscopy (SEM, Sigma 500, Oberkochen, Germany) equipped with an EDS system. The hollow structure was also observed with high resolution transmission electron microscope (HRTEM, JEM-2100F, JEOL, Tokyo, Japan). X-ray diffraction (XRD) patterns of materials were acquired by Bruker D8 Discover (Karlsruhe, Germany) diffractometer with the 2θ of 10–60° using Cu-Kα radiation source. The content of sulfur was measured by Thermogravimetric Analysis (TGA, Perkin Elmer, Series7, Waltham, MA, USA) in N_2 from 10 °C to 600 °C. The specific surface area and pore distribution calculation were measured by a V-Sorb 2800P analyzer instrument. The surface functional characteristics were analyzed by X-ray spectroscopy (XPS, ESCALAB 250Xi, Thermo Fisher Scientific, Waltham, MA, USA). The pore distribution of the samples was analyzed by Hg porosimetry by Mike Auto Pore IV 9500 (Norcross, GA, USA).

2.3. Electrochemical Measurements

The cathode was prepared by homogeneously mixing the S/$Ni(OH)_2$@CNT composites, PVDF, and acetylene black with a mass ratio of 8:1:1. The discharge/charge capacity is provided by the active material (sulfur), and the test electrode contains about 0.8–1.0 mg cm^{-2} of the active material [44]. Lithium foils were used as the anode and porous polypropylene (Celgard 2300) was used as the separator. A UV-Vis spectrophotometer (Perkin Elmer) was adopted to analyze the adsorption capability of samples to Li_2S_6 [45]. At room temperature, a BTS4000 battery testing system (Neware, Shenzhen, China) was used to test the battery for galvanostatic discharge/charge performance. The electrochemical impedance spectroscopy (EIS) and cyclic voltammetry (CV) were both performed on a CHI-660E electrochemical workstation (Chenhua, Yangzhou, China).

2.4. Theoretical Calculations

To further verify the adsorption effect of $Ni(OH)_2$ on LiPS, the binding energy (Ebind) between $Ni(OH)_2$ and LiPS was calculated by density functional theory (DFT), calculated by the following equation [46]:

$$E_{bind} = E_{total} - E_{LiPS} - E_{Ni(OH)_2}$$

where, E_{total}, E_{LiPS} and $E_{Ni(OH)_2}$ represent the energy of the corresponding substances. The magnitude of the binding capacity is positively correlated with the absolute value of E_{bind}.

3. Results and Discussion

The XRD patterns of composites were displayed in Figure 1a. Both XRD patterns of the $Ni(OH)_2$ and $Ni(OH)_2$@CNT composite show three clearly characteristic peaks located at 19.8°, 34° and 39.1°, which correspond to (001), (100) and (012) lattice planes of $Ni(OH)_2$ (JCPDS No.73-1520), respectively [47]. The sharp diffraction peaks demonstrated the good crystallinity of the as-synthesized $Ni(OH)_2$ precursor. A typical peak at about 26° observed in CNT belongs to the (002) plane of carbon [48–50]. The crystal plane was basically in line with the standard card. As expected, it was suggesting that the carbon nanotube decorated $Ni(OH)_2$ composites were prepared successfully.

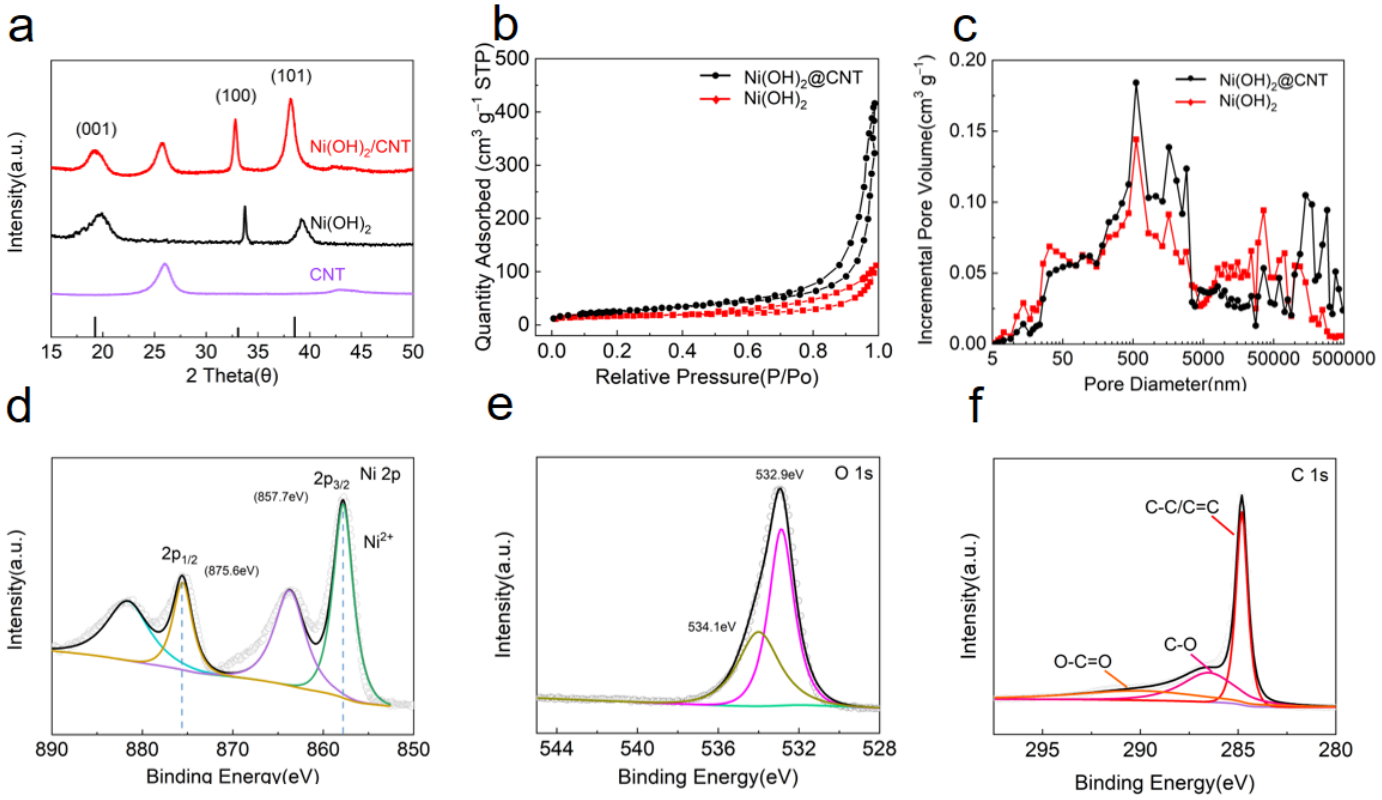

Figure 1. (**a**) XRD patterns of $Ni(OH)_2$@CNT, $Ni(OH)_2$ and CNT; (**b**) N_2 adsorption-desorption isotherms of $Ni(OH)_2$ and $Ni(OH)_2$@CNT. (**c**) The pore size distribution of $Ni(OH)_2$ and $Ni(OH)_2$@CNT. The XPS spectra of (**d**) Ni 2p, (**e**) O 1s, and (**f**) C 1s of $Ni(OH)_2$@CNT.

Furthermore, the N_2 adsorption-desorption isotherm was used to analyze pore characteristics (Figure 1b). $Ni(OH)_2$@CNT exhibits a higher specific surface area than $Ni(OH)_2$. In order to better understand the porosity of $Ni(OH)_2$@CNT composite materials, the Hg porosity measurement method was used to analyze the pore size distribution of $Ni(OH)_2$@CNT materials (Figure 1c). The pore volumes of $Ni(OH)_2$ and $Ni(OH)_2$@CNT composites are measured to be 3.37 $cm^3\ g^{-1}$ and 3.71 $cm^3\ g^{-1}$, respectively. Compared with $Ni(OH)_2$, the $Ni(OH)_2$@CNT composite has a higher macropore distribution. These results indicate that the large specific surface area and pore size distribution of $Ni(OH)_2$@CNT composites satisfy the premise of high sulfur loading. In addition, the hollow structure and outer nanosheets of $Ni(OH)_2$@CNTs can provide abundant pores and larger active interfaces, enabling faster ion/electron transportation and facilitating redox reactions.

To further validate the chemical states of $Ni(OH)_2$@CNT composite, XPS measurements were performed. The positions of all peaks are calibrated with the binding energy of 284.8 eV reported in the literature to standardize the energy of the instrument [51,52]. The high-resolution spectrum of Ni 2p (Figure 1d), showing two spin-orbit peaks and their satellite peaks. The presence of $Ni(OH)_2$ could be proved by the two spin-orbit peaks locating at 875.6 eV (Ni $2p_{1/2}$) and 857.7 eV (Ni $2p_{3/2}$). The Ni 2p spectrum was mainly composed of Ni^{2+}, which could inhibit the dissolution of LiPSs through chemical interaction with LiPSs. In the O 1s spectrum (Figure 1e), the peaks at 532.9 eV and 534.1 eV correspond to metal-OH bonds and C=O groups, respectively [53]. The three sub-peaks of the C 1s XPS spectrum (Figure 1f) are located at 284.8 eV, 286.51 eV and 290.21 eV, corresponding to C-C/C=C, C-O and O-C=O bonds, respectively. As shown in Figure S2a, all the elements of S, Ni, and O were detected by XPS on S/$Ni(OH)_2$@CNT. The Ni 2p spectrum (Figure S2b) displays four main peaks, which are in accord with the Ni 2p in $Ni(OH)_2$@CNT. The deconvolution of the S $2p_{3/2}$ spectrum (Figure S2c) revealed peaks located at 162.9 eV, 164.2 eV and 169.5 eV, which could be assigned to S^{2-}, S^0 and SO_x^{2-}

species, respectively. For the O 1s (Figure S2d), an intense band at 531.7 eV is obviously observed, which is considered to be the O from the OH^-. A low peak at 533.2 eV can be observed in the O 1s spectrum due to the influence of carbonate ions and hydroxyl groups.

According to the SEM image shown in Figure 2a, the synthesized $Ni(OH)_2$ exhibited a spherical morphology. SEM image demonstrated that the nanosheets are uniformly tightly anchored onto the surface of the nanoscale hollow spheres. This structure effectively avoided the loss of LiPSs. At the same time, the close contact of the nanosheet shell provided a guarantee for electron transfer of the electrode. The SEM image of the $Ni(OH)_2$@CNT obtained was shown in Figure 2b. It can be clearly seen that the spherical structure of composite was not impaired and the smooth surfaces became rough, which may be caused by the CNTs. As shown in the TEM image (Figure 2c), the $Ni(OH)_2$@CNT nanosheets possessed abundant void spaces, which can provide rich chemical reaction active sites. The crystalline feature of the $Ni(OH)_2$@CNT was further proved by HRTEM. The (100) plane of $Ni(OH)_2$ shown in Figure 2d was established by inverse fast Fourier transform (IFFT) patterns. Figure 2e,f shows the IFFT lattice image, where the fringe spaces of selected areas respectively are 0.226 nm (blue frame) and 0.224 nm (green frame), corresponding to the (100) planar spacing of $Ni(OH)_2$. Furthermore, elemental mapping images manifested the elemental homogeneous distribution of Ni, O and C in $Ni(OH)_2$@CNT (Figure 2g–j).

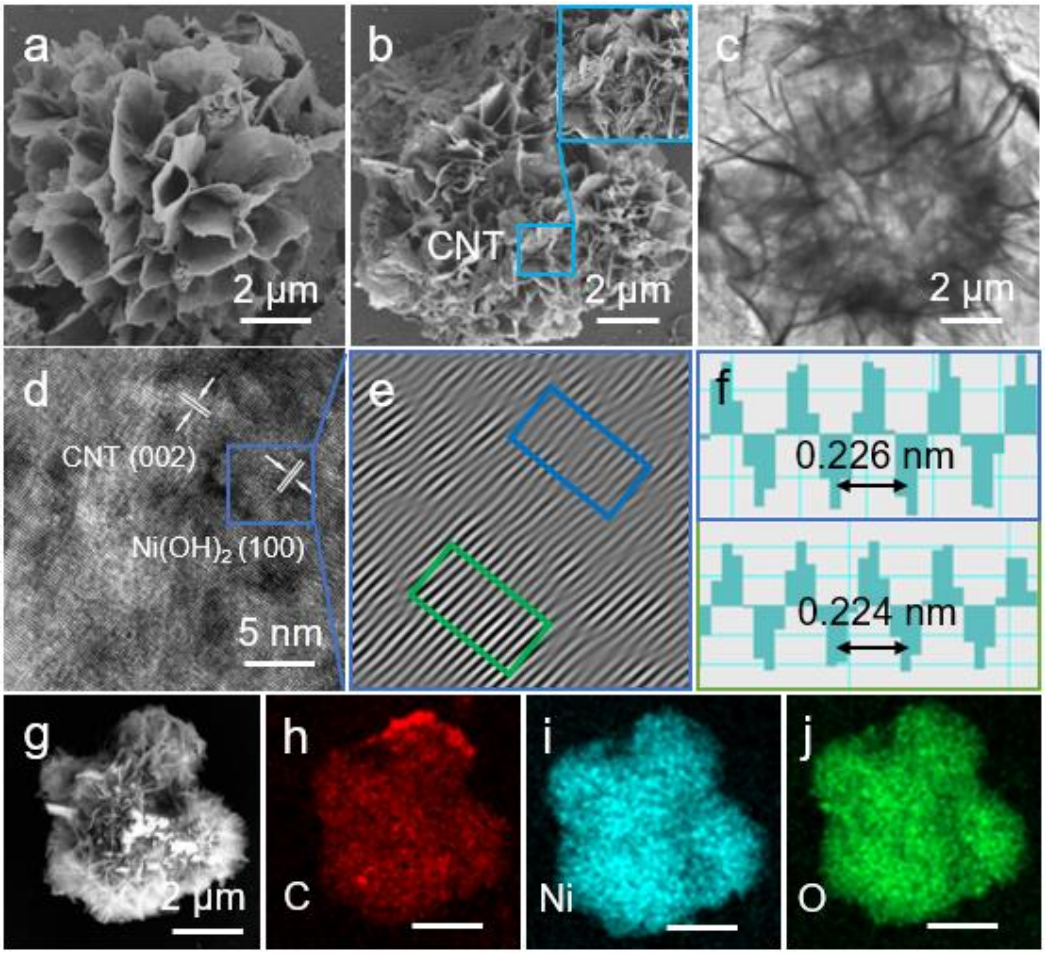

Figure 2. SEM image of $Ni(OH)_2$ (**a**); SEM and TEM images of $Ni(OH)_2$@CNT (**b**,**c**); (**d**) HRTEM image of $Ni(OH)_2$@CNT; (**e**,**f**) inverse FFT pattern and the corresponding lattice spacing profiles; (**g**–**j**) elemental mapping of $Ni(OH)_2$@CNT.

TGA was employed to analyze the sulfur content in composites (Figure 3). Three distinct phases of weightlessness are observed on the TGA plots. The first major weightlessness cause of the evaporation of embedded water molecules at around 50 °C. The

following loss occurs for the transformation from $Ni(OH)_2$ to NiO at ~220 °C. The third weightlessness occurred when NiO_2 is reductive decomposed at high temperatures above 400 °C. Due to the low content of $Ni(OH)_2$ in S/$Ni(OH)_2$@CNT, the loss was relatively small, which can be neglected. TGA plots shows an extremely fast weight loss between 160 and 300 °C, corresponding to the rapid sublimation of sulfur in the composite. The sulfur content in the S/$Ni(OH)_2$@CNT and S/$Ni(OH)_2$ composites is determined to be about 74.6 wt% and 66.9 wt% through the TGA, respectively. Under the same S: Samples ratio, the S content obtained in the experiment of this paper has a higher loading (Table S1, Supporting Information).

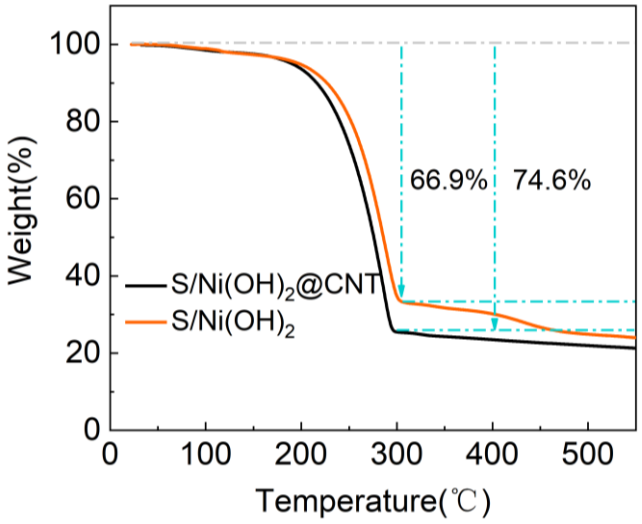

Figure 3. TGA curves of S/$Ni(OH)_2$ and S/$Ni(OH)_2$@CNT.

All electrochemical performance tests use CR2032-type coin cells. As shown in Figure 4a, one oxidation peak and two reduction peaks appear in the CV curves. In the cathodic reaction, the peak located at 2.14 V represented the formation of soluble polysulfides (Li_2S_n, $4 \leq n \leq 8$), the reduction of LiPSs to low-order LiPSs were associated with the cathodic peak at around 1.96 V. During the anodic cycle, only a sharp peak was shown at ~2.56 V, which is attributed to the chemical transformation from Li_2S to sulfur [54,55]. The nearly overlapped CV plots in the three cycles for the S/$Ni(OH)_2$@CNT indicated its highly electrochemical stability. The sharp and overlapped peaks indicated the high conductivity, high reaction stability and fast kinetics granted by S/$Ni(OH)_2$@CNT electrodes. Figure 4b displayed the discharge/charge curves for the S/$Ni(OH)_2$@CNT electrodes. Typical reaction plateaus were shown and were identical with the CV curves. The hollow structure and high conductivity of the S/$Ni(OH)_2$@CNT electrode rendered small polarization and high sulfur utilization. Moreover, the S/$Ni(OH)_2$@CNT electrode exhibits an initial specific capacity of 1146 mAh g^{-1} at 0.2 C with an initial coulombic efficiency of 98.1%. The cycling performance of different electrodes at 0.2 C is shown in Figure 4c. S/$Ni(OH)_2$@CNT exhibited an initial discharge capacity of 1146 mAh g^{-1}, indicating a good sulfur utilization. After 100 cycles, the capacity retention of S/$Ni(OH)_2$@CNT cathode is 83.4%, which is larger than S/$Ni(OH)_2$ (689 mAh g^{-1}) and S/CNT (483 mAh g^{-1}) electrodes.

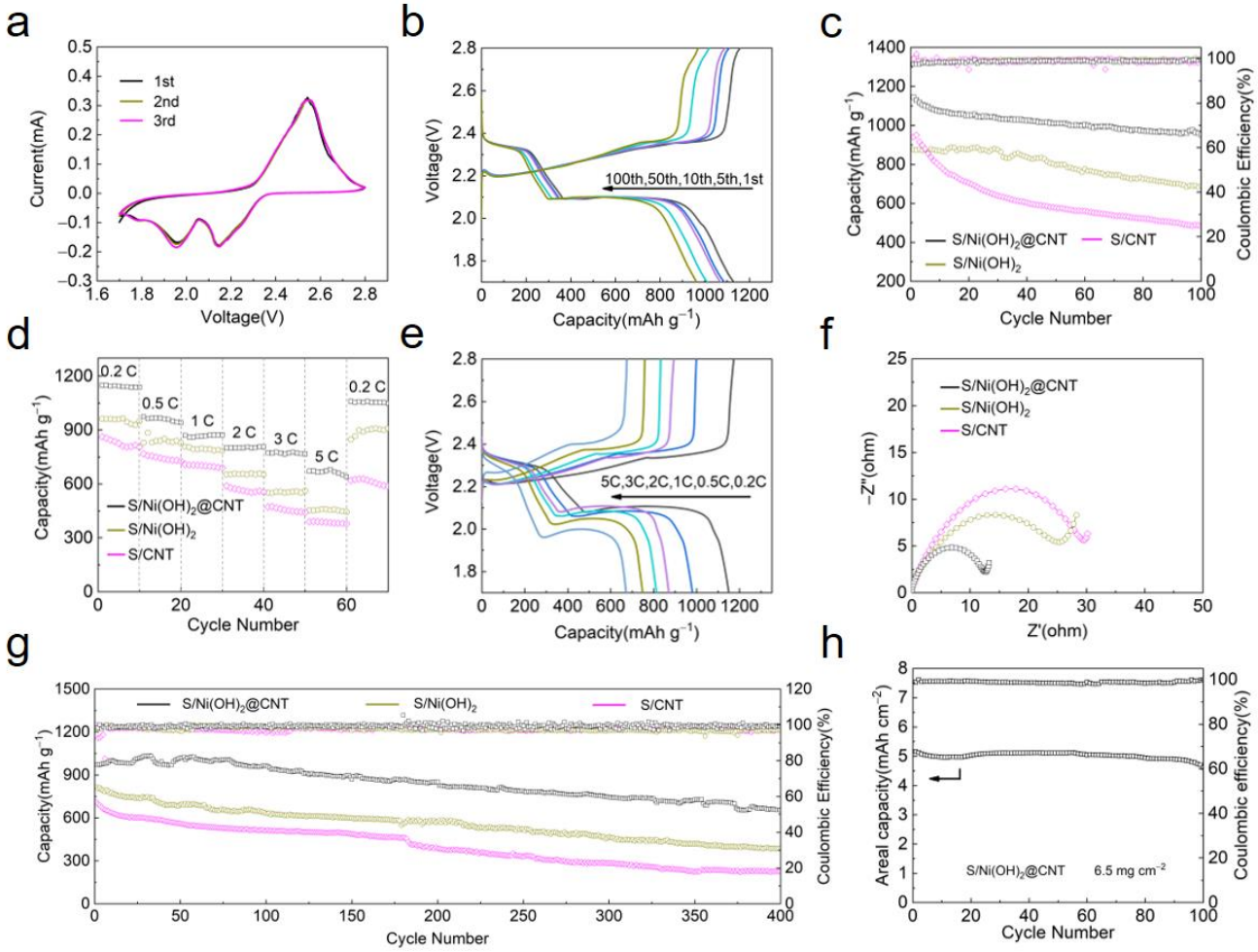

Figure 4. (**a**) Cycle voltammograms of Li-S batteries with S/Ni(OH)$_2$@CNT cathodes; (**b**) discharge/charge curves at 0.2 C; (**c**) Cycling performance with different electrodes at 0.2 C; rate capability (**d**,**e**) profiles of S/Ni(OH)$_2$@CNT cathode at various current rates between 0.2 and 5 C; (**f**) EIS spectra of batteries with the different electrodes; (**g**) long term cycling performance of Li-S batteries with different electrodes at 1 C for 400 cycles; (**h**) cyclic stability of S/Ni(OH)$_2$@CNT cathode with high sulfur loading of 6.5 mg cm^{-2} at 0.2 C.

The S/Ni(OH)$_2$@CNT also delivered excellent rate performance (Figure 4d). After initial activation, the S/Ni(OH)$_2$@CNT electrode delivers 1148 mAh g^{-1} at 0.2 C. At 0.5, 1, 2, 3, and 5 C, the reversible capacities of Li-S batteries with the S/Ni(OH)$_2$@CNT electrode were around 974, 869, 801, 773, and 672 mAh g^{-1}, respectively. Moreover, when the discharge/charge rate was abruptly returned to 0.2 C, the capacity of S/Ni(OH)$_2$@CNT cathode recovered to 1054 mAh g^{-1}, confirming the outstanding cycling stability and structure robustness of the electrode. It was noteworthy that S/Ni(OH)$_2$@CNT cathode displayed a small plateau potential difference (ΔE) at all current densities (Figure 4e).

Electrochemical impedance spectra of the cells with S/CNT, S/Ni(OH)$_2$ and S/Ni(OH)$_2$ @CNT electrodes were conducted to investigate the difference of internal resistance, as shown in Figure 4f. Three Nyquist plots of the S/Ni(OH)$_2$@CNT, S/Ni(OH)$_2$, and S/CNT batteries were in the same shape consisting of one semicircle referring to the charge-transfer resistance (R_{ct}) and one sloped line associated with Li^+ diffusion process. The S/Ni(OH)$_2$@CNT cathode shows the lowest charge transfer resistance value (R_{ct} = 13 Ω) when compared with S/Ni(OH)$_2$ (R_{ct} = 25 Ω) and S/CNT (R_{ct} = 30 Ω), indicating that the battery with S/Ni(OH)$_2$@CNT cathode had the fastest charge transfer kinetics, which can be ascribe to the introduction of the S/Ni(OH)$_2$@CNT electrodes into Li-S batteries greatly enhanced the electronic conductivity and reaction kinetics.

Long-term cycling test at 1 C was further performed on the S/$Ni(OH)_2$@CNT, S/$Ni(OH)_2$ and S/CNT cathode (Figure 4g). The S/$Ni(OH)_2$@CNT provided a high capacity of 972 mAh g^{-1} at 1 C. The discharge capacity exhibited an evident increase in the first 50 cycles. The S/$Ni(OH)_2$@CNT cathode was gradually infiltrated by the electrolyte, so the active material can be effectively utilized. After 400 cycles, the discharge capacity was 652 mAh g^{-1}, which meant the capacity loss per cycle was only 0.081%.

To demonstrate the potential of the S/$Ni(OH)_2$@CNT in the high energy density Li-S battery, the cycling property of Li-S Batteries with high sulfur loadings was tested. As shown in Figure 4h, the S/$Ni(OH)_2$@CNT electrode exhibits a stable high areal capacity of 4.6 mAh cm^{-2} and an energy density of 1679.4 Wh Kg^{-1} (Figure S3) even at a high sulfur loading of 6.5 mg cm^{-2}. Besides, the performance advantages of as-developed S/$Ni(OH)_2$@CNT electrode can also be confirmed from the comparison with recently reported carbon-based electrodes (Table S1, Supporting Information).

Generally speaking, if the Li_2S_2 and Li_2S cannot be converted completely and quickly at a high rate, they would gradually deposit on the surface of the electrode and block the reaction channel between electrons and lithium ions. The $Ni(OH)_2$ with a nano-sheet structure can accelerate the diffusion of electrons/lithium ions, while preventing the polysulfides from dissolving during the cycling process. Among the various LiPSs, trapping the Li_2S_6 and Li_2S_4 species within the cathode matrix was crucial. To intuitively verify the adsorption ability of $Ni(OH)_2$ to LiPSs, the polysulfide (Li_2S_6) adsorption tests have been carried out on the $Ni(OH)_2$@CNT. As the inset in Figure 5a, 50 mg of $Ni(OH)_2$@CNT, $Ni(OH)_2$ and CNT were placed in a THF solution containing 0.05 M Li_2S_6, respectively. After standing for 12 h, the color of the Li_2S_6 solution with $Ni(OH)_2$@CNT became colorless to further illustrate the affinity of $Ni(OH)_2$@CNT for LiPSs. According to the UV-vis spectra, in the polysulfide solution, S_6^{2-} had a characteristic peak, located at 278 nm. Obviously, after adding $Ni(OH)_2$@CNT to the simulated solution, the intensity of the S_6^{2-} peak dropped sharply. $Ni(OH)_2$@CNT demonstrated a remarkable ability to absorb Li_2S_6, which is consistent with the above observation.

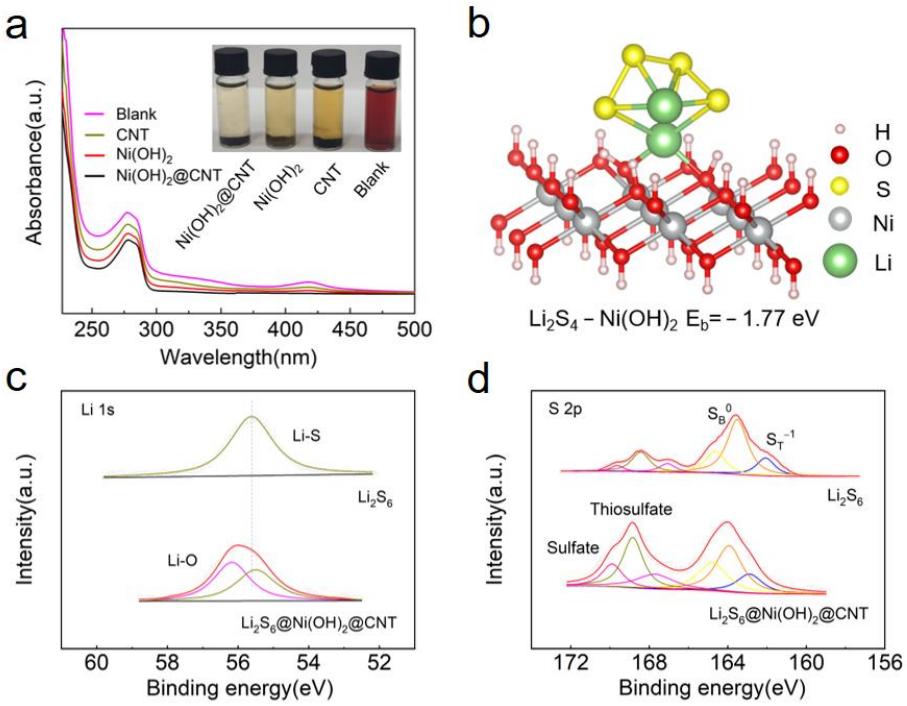

Figure 5. (**a**) Optical observation of LiPS adsorption by CNT, $Ni(OH)_2$, $Ni(OH)_2$@CNT and the corresponding UV–vis spectra. (**b**) optimized configuration and the corresponding binding energy of Li_2S_4 on $Ni(OH)_2$@CNT surfaces. (**c**) Li 1s and (**d**) S 2p spectra of Li_2S_6 before and after adsorbed on $Ni(OH)_2$@CNT.

To further confirm the strong chemisorption of $Ni(OH)_2$ on LiPS, the binding energy of Li_2S_4 on $Ni(OH)_2$ was studied using density functional theory (DFT) calculations. Figure 5b shows the geometrically stable configuration of Li_2S_4 adsorbed on $Ni(OH)_2$, in which there is a "lithium bond"-like bridge. Adsorption configurations of Li_2S_4 on $Ni(OH)_2$ were showed with a binding energy of −1.77 eV, which indicates that $Ni(OH)_2$ presents significantly adsorption capacity for LiPS. Moreover, the interaction between $Ni(OH)_2$@CNT and LiPS $Ni(OH)_2$@CNT was also studied by XPS analysis. The peak at 56.2 eV of the Li_2S_6@$Ni(OH)_2$@CNT indicates the formation of Li-O bonds (Figure 5c). Figure 5d shows the S 2p spectrum of bare Li_2S_6, where the two pairs of peaks at 162.1 and 163.5 eV correspond to the terminal S and bridging S, respectively. After interaction with $Ni(OH)_2$@CNT, these peaks showed a considerable shift to the higher binding energy (BE) range, indicating that the electron cloud density of sulfur atoms decreases after adsorption of $Ni(OH)_2$@CNT. The result demonstrated that $Ni(OH)_2$@CNT had strong chemical and physical absorbing ability, which inhibit the effects of LiPSs, and were significant to the confinement of the shuttle effect.

4. Conclusions

In summary, we report a Li-S battery using $Ni(OH)_2$@CNT with hierarchical intersecting hollow structures as sulfur carriers. First, it accelerates electron/lithium–ion diffusion and prevents LiPSs from dissolving during the cycle. A cooperative interface is composed of "physical confinement" and "chemical adsorption" to effectively capture LiPSs and facilitate the reaction kinetics. Furthermore, the introduction of these abundant functional polar/hydrophilic groups of $Ni(OH)_2$@CNT could restrict the shuttle effect of LiPSs through strong chemical adsorption. Finally, the compact structure of the S/$Ni(OH)_2$@CNT cathode keeps the sulfur safely confined to micro-pores. This work sheds light on the promising practical applications of transition metal hydroxide in Li-S batteries.

Supplementary Materials: The following are available online at https://www.mdpi.com/article/10.3390/nano12050886/s1, Figure S1. SEM images of S/$Ni(OH)_2$@CNT; Figure S2. (a) XPS survey and high-resolution (b) Ni 2p, (c) S 2p, and (d) O 1s spectra of S/$Ni(OH)_2$@CNT; Figure S3. Energy density of S/$Ni(OH)_2$@CNT cathode with high sulfur loading of 6.5 mg cm^{-2} at 0.2 C; Table S1. Sulfur loading comparison of S/$Ni(OH)_2$@CNT with previously reported S/C cathodes; Table S2. Performance comparison among different C-based sulfur electrodes. References [56–66] were cited in the supplementary materials.

Author Contributions: Methodology, Q.J.; formal analysis, Q.J. and Y.Y.; investigation, Q.J. and C.H.; writing—original draft preparation, Q.J.; writing—review and editing, Y.Z., X.W. and C.L.; supervision, Y.Z. and C.L.; project administration, Y.Z. and X.W.; funding acquisition, Y.Z. All authors have read and agreed to the published version of the manuscript.

Funding: This research was funded by Natural Science Foundation of Hebei Province of China (B2021202028; B2020202052); National Key R&D Program of China (No.2019YFC1908504); State Key Laboratory of Reliability and Intelligence of Electrical Equipment (No. EERI_PI2020007), Hebei University of Technology, China; the Program for the Outstanding Young Talents of Hebei Province, China (YG.Z.); Chunhui Project of Ministry of Education of the People's Republic of China (No. Z2017010).

Institutional Review Board Statement: Not applicable.

Informed Consent Statement: Not applicable.

Data Availability Statement: Data are contained within the article.

Conflicts of Interest: The authors declare no conflict of interest.

References

1. Razzaq, A.A.; Yuan, X.T.; Chen, Y.J.; Hu, J.P.; Mu, Q.Q.; Ma, Y.; Zhao, X.H.; Miao, L.X.; Ahn, J.H.; Peng, Y.; et al. Anchoring MOF-derived CoS2 on sulfurized polyacrylonitrile nanofibers for high areal capacity lithium–sulfur batteries. *J. Mater. Chem. A* **2020**, *8*, 1298–1306. [CrossRef]
2. Baumann, A.E.; Downing, J.R.; Burns, D.A.; Hersam, M.C.; Thoi, V.S. Graphene-Metal-Organic Framework Composite Sulfur Electrodes for Li-S Batteries with High Volumetric Capacity. *ACS Appl. Mater. Interfaces* **2020**, *12*, 37173–37181. [CrossRef]
3. Cai, R.Z.; Chen, X.X.; Liu, P.G.; Chen, T.; Liu, W.W.; Fan, X.W.; Ouyang, B.X.; Liu, K.Y. A Novel Cathode Based on Selenium Confined in Biomass Carbon and Graphene Oxide for Potassium-Selenium Battery. *ChemElectroChem* **2020**, *7*, 4477–4483. [CrossRef]
4. Chen, S.X.; Luo, J.H.; Li, N.Y.; Han, X.X.; Wang, J.; Deng, Q.; Zeng, Z.L.; Deng, S.G. Multifunctional LDH/Co_9S_8 heterostructure nanocages as high-performance lithium–sulfur battery cathodes with ultralong lifespan. *Energy Storage Mater.* **2020**, *30*, 187–195. [CrossRef]
5. Chiochan, P.; Kosasang, S.; Ma, N.; Duangdangchote, S.; Suktha, P.; Sawangphruk, M. Confining Li_2S_6 catholyte in 3D graphene sponge with ultrahigh total pore volume and oxygen-containing groups for lithium-sulfur batteries. *Carbon* **2020**, *158*, 244–255. [CrossRef]
6. Dai, C.L.; Hu, L.Y.; Wang, M.Q.; Chen, Y.M.; Han, J.; Jiang, J.; Zhang, Y.; Shen, B.; Niu, Y.B.; Bao, S.J.; et al. Uniform α-$Ni(OH)_2$ hollow spheres constructed from ultrathin nanosheets as efficient polysulfide mediator for long-term lithium-sulfur batteries. *Energy Storage Mater.* **2017**, *8*, 202–208. [CrossRef]
7. Dong, W.; Meng, L.Q.; Hong, X.D.; Liu, S.Z.; Shen, D.S.; Xia, Y.K.; Yang, S.B. MnO_2/rGO/CNTs Framework as a Sulfur Host for High-Performance Li-S Batteries. *Molecules* **2020**, *25*, 1989. [CrossRef]
8. Gu, X.X.; Tong, C.J.; Wen, B.; Liu, L.M.; Lai, C.; Zhang, S.Q. Ball-milling synthesis of ZnO@sulphur/carbon nanotubes and $Ni(OH)_2$@sulphur/carbon nanotubes composites for high-performance lithium-sulphur batteries. *Electrochim. Acta* **2016**, *196*, 369–376. [CrossRef]
9. Guo, J.W.; Wu, M.S. Carbon paper with attached hollow mesoporous nickel oxide microspheres as a sulfur-hosting material for rechargeable lithium-sulfur batteries. *Electrochim. Acta* **2019**, *327*, 135028. [CrossRef]
10. Han, K.R.; Wang, T.; Zhang, N.; Zhang, W.M.; Ge, W.Q.; Xie, G.; Zhang, L.P.; Zhang, T.Z. A film coating assembled by tubular nitrogen-doped carbon fibers as an efficient membrane spacer to suppress the shuttle effect for long-life lithium–sulfur batteries. *Electrochim. Acta* **2021**, *365*, 137232. [CrossRef]
11. Li, C.; Zhao, Y.; Zhang, Y.; Luo, D.; Liu, J.; Wang, T.; Gao, W.; Li, H.; Wang, X. A new defect-rich and ultrathin ZnCo layered double hydroxide/carbon nanotubes architecture to facilitate catalytic conversion of polysulfides for high-performance Li-S batteries. *Chem. Eng. J.* **2021**, *417*, 129248. [CrossRef]
12. Zhang, Y.G.; Zhao, Y.; Bakenov, Z.A. simple approach to synthesize nanosized sulfur/graphene oxide materials for high-performance lithium/sulfur batteries. *Ionics* **2014**, *20*, 1047–1050. [CrossRef]
13. Liu, R.Q.; Liu, Z.W.; Liu, W.H.; Liu, Y.J.; Lin, X.J.; Li, Y.; Li, P.; Huang, Z.D.; Feng, X.M.; Yu, L.S.; et al. TiO_2 and Co Nanoparticle-Decorated Carbon Polyhedra as Efficient Sulfur Host for High-Performance Lithium-Sulfur Batteries. *Small* **2019**, *15*, e1804533. [CrossRef] [PubMed]
14. Liu, X.H.; Qian, X.J.; Tang, W.Q.; Luo, H.; Zhao, Y.; Tan, R.; Qiao, M.; Gao, X.L.; Hua, Y.; Wang, H.Z.; et al. Designer uniform Li plating/stripping through lithium–cobalt alloying hierarchical scaffolds for scalable high-performance lithium-metal anodes. *J. Energy Chem.* **2021**, *52*, 385–392. [CrossRef]
15. Liu, X.; Wang, S.; Wang, A.L.; Wang, Z.N.; Chen, J.; Zeng, Q.H.; Chen, P.P.; Liu, W.; Li, Z.X.; Zhang, L.Y. A new cathode material synthesized by a thiol-modified metal–organic framework (MOF) covalently connecting sulfur for superior long-cycling stability in lithium–sulfur batteries. *J. Mater. Chem. A* **2019**, *7*, 24515–24523. [CrossRef]
16. Ren, J.; Song, Z.C.; Zhou, X.M.; Chai, Y.R.; Lu, X.L.; Zheng, Q.J.; Xu, C.G.; Lin, D.M. A Porous Carbon Polyhedron/Carbon Nanotube Based Hybrid Material as Multifunctional Sulfur Host for High-Performance Lithium-Sulfur Batteries. *ChemElectroChem* **2019**, *6*, 3410–3419. [CrossRef]
17. Li, Z.; Yuan, L.X.; Yi, Z.Q.; Sun, Y.M.; Liu, Y.; Jiang, Y.; Shen, Y.; Xin, Y.; Zhang, Z.L.; Huang, Y.H. Insight into the Electrode Mechanism in Lithium-Sulfur Batteries with Ordered Microporous Carbon Confined Sulfur as the Cathode. *Adv. Energy Mater.* **2014**, *4*, 1301473. [CrossRef]
18. Ousmane, I.A.M.; Li, R.; Wang, C.; Li, G.R.; Cai, W.L.; Liu, B.H.; Li, Z.P. Fabrication of oriented-macroporous-carbon incorporated with γ-Al_2O_3 for high performance lithium-sulfur battery. *Microporous Mesoporous Mat.* **2018**, *266*, 276–282. [CrossRef]
19. Seo, S.D.; Park, D.J.; Park, S.B.; Kim, D.W. "Brain-Coral-Like" Mesoporous Hollow CoS_2@N-Doped Graphitic Carbon Nanoshells as Efficient Sulfur Reservoirs for Lithium–Sulfur Batteries. *Adv. Funct. Mater.* **2019**, *29*, 1903712. [CrossRef]
20. Zhang, Y.G.; Qiu, W.L.; Zhao, Y.; Wang, Y.; Bakenov, Z.; Wang, X. Ultra-fine zinc oxide nanocrystals decorated three-dimensional macroporous polypyrrole inverse opal as efficient sulfur hosts for lithium/sulfur batteries. *Chem. Eng. J.* **2019**, *375*, 122055. [CrossRef]
21. Zhang, Y.G.; Bakenov, Z.; Zhao, Y.; Konarov, A.; Wang, Q.; Chen, P. Three-dimensional carbon fiber as current collector for lithium/sulfur batteries. *Ionics* **2013**, *20*, 803–808. [CrossRef]

22. Li, Y.; Zhu, J.D.; Shi, R.W.; Dirican, M.; Zhu, P.; Yan, C.Y.; Jia, H.; Zang, J.; He, J.H.; Zhang, X.W. Ultrafine and polar ZrO_2-inlaid porous nitrogen-doped carbon nanofiber as efficient polysulfide absorbent for high-performance lithium-sulfur batteries with long lifespan. *Chem. Eng. J.* **2018**, *349*, 376–387. [CrossRef]
23. Wang, J.Y.; Wang, W.J.; Zhang, Y.G.; Wang, Y.; Zhao, Y. Synthesis of CoO nanocrystals decorated porous carbon nanotube microspheres as sulfur host for high performance Li/S batteries. *Nanotechnology* **2020**, *31*, 025403. [CrossRef] [PubMed]
24. Wu, H.; Jiang, H.; Yang, Y.Q.; Hou, C.Y.; Zhao, H.T.; Xiao, R.; Wang, H.Z. Cobalt nitride nanoparticle coated hollow carbon spheres with nitrogen vacancies as an electrocatalyst for lithium–sulfur batteries. *J. Mater. Chem. A* **2020**, *8*, 14498–14505. [CrossRef]
25. Wu, H.L.; Li, Y.; Ren, J.; Rao, D.W.; Zheng, Q.J.; Zhou, L.; Lin, D.M. CNT-assembled dodecahedra core@nickel hydroxide nanosheet shell enabled sulfur cathode for high-performance lithium-sulfur batteries. *Nano Energy* **2019**, *55*, 82–92. [CrossRef]
26. Wu, Q.P.; Zhou, X.J.; Xu, J.; Cao, F.H.; Li, C.L. Carbon-based derivatives from metal-organic frameworks as cathode hosts for Li–S batteries. *J. Energy Chem.* **2019**, *38*, 94–113. [CrossRef]
27. Xia, Y.; Zhong, H.Y.; Fang, R.Y.; Liang, C.; Xiao, Z.; Huang, H.; Gan, Y.P.; Zhang, J.; Tao, X.Y.; Zhang, W.K. Biomass derived $Ni(OH)_2$@porous carbon/sulfur composites synthesized by a novel sulfur impregnation strategy based on supercritical CO_2 technology for advanced Li-S batteries. *J. Power Sources* **2018**, *378*, 73–80. [CrossRef]
28. Liu, P.; Zhong, W.; Du, W.Y.; Guo, B.S.; Qi, Y.R.; Bao, S.J.; Xu, M.W. Suppressed shuttling effect of polysulfides using three-dimensional nickel hydroxide polyhedrons for advanced lithium-sulfur batteries. *J. Colloid Interface Sci.* **2021**, *593*, 89–95. [CrossRef]
29. Zhao, C.F.; Ge, F.; Shi, L.W.; Wang, H.; Liu, J.L.; Zhang, J.F.; Hou, S.F.; Yu, H.J.; Hu, C. Graphene–sulfur–$Ni(OH)_2$ sandwich foam composites as free-standing cathodes for high-performance Li–S batteries. *Int. J. Hydrogen Energy* **2019**, *44*, 30478–30485. [CrossRef]
30. Zhang, Y.G.; Zhao, Y.; Konarov, A.; Gosselink, D.; Li, Z.; Ghaznavi, M.; Chen, P. One-pot approach to synthesize PPy@S core–shell nanocomposite cathode for Li/S batteries. *J. Nanopart. Res.* **2013**, *15*, 1–7. [CrossRef]
31. Zhao, J.G. $Ni(OH)_2$@hollow carbon spheres/sulfur composites as cathode materials for high-performance Li–S batteries. *J. Mater. Sci.-Mater. Electron.* **2019**, *30*, 17155–17163. [CrossRef]
32. Zheng, S.; Zhang, H.Y.; Fan, J.C.; Xu, Q.J.; Min, Y.L. Improving Electrochemical Performance and Safety of Lithium-Sulfur Batteries by a "Bulletproof Vest". *ACS Appl. Mater. Interfaces* **2020**, *12*, 51904–51916. [CrossRef] [PubMed]
33. Shi, Z.J.; Feng, W.J.; Wang, X.; Li, M.M.; Song, C.K.; Chen, L.J. Catalytic cobalt phosphide Co_2P/carbon nanotube nanocomposite as host material for high performance lithium-sulfur battery cathode. *J. Alloys Compd.* **2021**, *851*, 156289. [CrossRef]
34. Wang, G.; Feng, Y.; Chen, J.Y.; Ju, J.G.; Zhang, S.P.; Zhao, Y.X.; Cheng, B.W.; Fan, J.; Li, L.; Deng, N.P.; et al. Mg-Al layered double hydroxides modified N-doped porous carbon nanofibers film as cathodic interlayer for high performance Li-S batteries. *J. Alloys Compd.* **2021**, *875*, 160073. [CrossRef]
35. Shi, H.D.; Dong, Y.F.; Zhou, F.; Chen, J.; Wu, Z.S. 2D hybrid interlayer of electrochemically exfoliated graphene and $Co(OH)_2$ nanosheet as a bi-functionalized polysulfide barrier for high-performance lithium–sulfur batteries. *J. Phys.-Energy* **2018**, *1*, 015002. [CrossRef]
36. Shi, W.H.; Mao, J.; Xu, X.L.; Liu, W.X.; Zhang, L.; Cao, X.H.; Lu, X.H. An ultra-dense NiS_2/reduced graphene oxide composite cathode for high-volumetric/gravimetric energy density nickel–zinc batteries. *J. Mater. Chem. A.* **2019**, *7*, 15654–15661. [CrossRef]
37. Wu, T.; Sun, G.R.; Lu, W.; Zhao, L.P.; Mauger, A.; Julien, C.M.; Sun, L.Q.; Xie, H.M.; Liu, J.H. A polypyrrole/black-TiO_2/S double-shelled composite fixing polysulfides for lithium-sulfur batteries. *Electrochim. Acta* **2020**, *353*, 136529. [CrossRef]
38. Zhang, R.H.; Wu, M.C.; Fan, X.Z.; Jiang, H.R.; Zhao, T.S. A Li-S battery with ultrahigh cycling stability and enhanced rate capability based on novel ZnO yolk-shell sulfur host. *J. Energy Chem.* **2021**, *55*, 136–144. [CrossRef]
39. Geng, X.W.; Yi, R.W.; Lin, X.F.; Liu, C.G.; Sun, Y.; Zhao, Y.C.; Li, Y.Q.; Mitrovic, I.; Liu, R.; Yang, L.; et al. A high conductive TiC–TiO_2/SWCNT/S composite with effective polysulfides adsorption for high performance Li–S batteries. *J. Alloys Compd.* **2021**, *851*, 156793. [CrossRef]
40. Feng, Y.Q.; Liu, H.; Zhao, F.W.; Liu, Y.; Li, J.Q.; Liu, X.X. Simultaneous defect-engineered and thiol modified of MoO_2 for improved catalytic activity in lithium-sulfur batteries: A study of synergistic polysulfide adsorption-conversion function. *Chem. Eng. J.* **2021**, *409*, 128177. [CrossRef]
41. Al-Tahan, M.A.; Dong, Y.T.; Zhang, R.; Zhang, Y.Y.; Zhang, J.M. Understanding the high-performance $Fe(OH)_3$@GO nanoarchitecture as effective sulfur hosts for the high capacity of lithium-sulfur batteries. *Appl. Surf. Sci.* **2021**, *538*, 148032. [CrossRef]
42. Deng, N.P.; Feng, Y.; Wang, G.; Wang, X.X.; Wang, L.Y.; Li, Q.X.; Zhang, L.T.; Kang, W.M.; Cheng, B.W.; Liu, Y. Rational structure designs of 2D materials and their applications toward advanced lithium-sulfur battery and lithium-selenium battery. *Chem. Eng. J.* **2020**, *401*, 125976. [CrossRef]
43. He, Y.S.; Li, M.J.; Zhang, Y.G.; Shan, Z.Z.; Zhao, Y.; Li, J.D.; Liu, G.H.; Liang, C.Y.; Bakenov, Z.; Li, Q. All-Purpose Electrode Design of Flexible Conductive Scaffold toward High-Performance Li–S Batteries. *Adv. Funct. Mater.* **2020**, *30*, 2000613. [CrossRef]
44. Qiu, W.L.; Li, G.R.; Luo, D.; Zhang, Y.G.; Zhao, Y.; Zhou, G.F.; Shui, L.L.; Wang, X.; Chen, Z.W. Hierarchical Micro-Nanoclusters of Bimetallic Layered Hydroxide Polyhedrons as Advanced Sulfur Reservoir for High-Performance Lithium-Sulfur Batteries. *Adv. Sci.* **2021**, *8*, 2003400. [CrossRef]
45. Zhang, Y.G.; Li, G.R.; Wang, J.Y.; Luo, D.; Sun, Z.H.; Zhao, Y.; Yu, A.P.; Wang, X.; Chen, Z.W. "Sauna" Activation toward Intrinsic Lattice Deficiency in Carbon Nanotube Microspheres for High-Energy and Long-Lasting Lithium–Sulfur Batteries. *Adv. Energy Mater.* **2021**, *11*, 2100497. [CrossRef]

46. Rojaee, R.; Shahbazian-Yassar, R. Two-Dimensional Materials to Address the Lithium Battery Challenges. *ACS Nano* **2020**, *14*, 2628–2658. [CrossRef]
47. Zhao, Z.M.; Zhao, J.W.; Hu, Z.L.; Li, J.D.; Li, J.J.; Zhang, Y.J.; Wang, C.; Cui, G.L. Long-life and deeply rechargeable aqueous Zn anodes enabled by a multifunctional brightener-inspired interphase. *Energy Environ. Sci.* **2019**, *12*, 1938–1949. [CrossRef]
48. Wang, N.N.; Wang, J.; Zhao, J.J.; Wang, J.H.; Pan, J.Q.; Huang, J.R. Synthesis of porous-carbon@reduced graphene oxide with superior electrochemical behaviors for lithium-sulfur batteries. *J. Alloys Compd.* **2021**, *851*, 156832. [CrossRef]
49. Park, J.H.; Choi, W.Y.; Yang, J.; Kim, D.; Gim, H.; Lee, J.W. Nitrogen-rich hierarchical porous carbon paper for a free-standing cathode of lithium sulfur battery. *Carbon* **2021**, *172*, 624–636. [CrossRef]
50. Zhang, Y.; Wan, F.; Huang, S.; Wang, S.; Niu, Z.Q.; Chen, J. A chemically self-charging aqueous zinc-ion battery. *Nat. Commun.* **2020**, *11*, 2199. [CrossRef]
51. Wang, T.; Cui, G.L.; Zhao, Y.; Nurpeissova, A.; Bakenov, Z. Porous carbon nanotubes microspheres decorated with strong catalyst cobalt nanoparticles as an effective sulfur host for lithium-sulfur battery. *J. Alloys Compd.* **2021**, *853*, 157268. [CrossRef]
52. Chen, L.P.; Yang, R.; Yan, Y.L.; Zou, Y.M.; Li, X.F.; Deng, Q.J.; Xu, Y.H. Controlling hydroxyl content of reduced graphene oxide for superior cathode performance of lithium sulfur batteries. *Electrochim. Acta* **2020**, *362*. [CrossRef]
53. Cui, Y.H.; Zhao, Q.H.; Wu, X.J.; Chen, X.; Yang, J.L.; Wang, Y.T.; Qin, R.Z.; Ding, S.X.; Song, Y.L.; Wu, J.W.; et al. An Interface-Bridged Organic-Inorganic Layer that Suppresses Dendrite Formation and Side Reactions for Ultra-Long-Life Aqueous Zinc Metal Anodes. *Angew. Chem.-Int. Edit.* **2020**, *59*, 16594–16601. [CrossRef] [PubMed]
54. Feng, Y.; Wang, G.; Kang, W.M.; Deng, N.P.; Cheng, B.W. Taming polysulfides and facilitating lithium-ion migration: Novel electrospinning MOFs@PVDF-based composite separator with spiderweb-like structure for Li-S batteries. *Electrochim. Acta* **2021**, *365*, 137344. [CrossRef]
55. Li, H.X.; Ma, S.; Li, J.W.; Liu, F.Y.; Zhou, H.H.; Huang, Z.Y.; Jiao, S.Q.; Kuang, Y.F. Altering the reaction mechanism to eliminate the shuttle effect in lithium-sulfur batteries. *Energy Storage Mater.* **2020**, *26*, 203–212. [CrossRef]
56. Hu, G.J.; Sun, Z.H.; Shi, C.; Fang, R.P.; Chen, J.; Hou, P.X.; Liu, C.; Cheng, H.M.; Li, F. A Sulfur-Rich Copolymer@CNT Hybrid Cathode with Dual-Confinement of Polysulfides for High-Performance Lithium-Sulfur Batteries. *Adv. Mater.* **2017**, *29*, 1603835. [CrossRef]
57. Song, Z.C.; Lu, X.L.; Li, X.Y.; Jiang, N.; Huo, Y.; Zheng, Q.J.; Lin, D.M. Tailored multifunctional hybrid cathode substrate configured with carbon nanotube-modified polar $Co(PO_3)_2$/CoP nanoparticles embedded nitrogen-doped porous-shell carbon polyhedron for high-performance lithium-sulfur batteries. *J. Colloid Interface Sci.* **2020**, *575*, 220–230. [CrossRef]
58. He, J.R.; Bhargav, A.; Yaghoobnejad Asl, H.; Chen, Y.F.; Manthiram, A. 1T′-ReS_2 Nanosheets In Situ Grown on Carbon Nanotubes as a Highly Efficient Polysulfide Electrocatalyst for Stable Li-S Batteries. *Adv. Energy Mater.* **2020**, *10*, 2001017. [CrossRef]
59. Niu, X.Q.; Wang, X.L.; Wang, D.H.; Li, Y.; Zhang, Y.J.; Zhang, Y.D.; Yang, T.; Yu, T.; Tu, J.P. Metal hydroxide - a new stabilizer for the construction of sulfur/carbon composites as high-performance cathode materials for lithium-sulfur batteries. *J. Mater. Chem. A.* **2015**, *3*, 17106–17112. [CrossRef]
60. Hwang, J.-Y.; Kim, H.M.; Shin, S.; Sun, Y.-K. Designing a High-Performance Lithium-Sulfur Batteries Based on Layered Double Hydroxides-Carbon Nanotubes Composite Cathode and a Dual-Functional Graphene-Polypropylene-Al_2O_3 Separator. *Adv. Funct. Mater.* **2018**, *28*, 1704294. [CrossRef]
61. Wu, Y.Q.; Luo, Z.X.; Wang, X.R.; Fu, G.L.; Lei, W.X.; Zou, Y.L.; Yin, B.B.; Ma, Z.S.; Pan, Y.; Jiang, W.J. Cotton-like CNTs/(Ni-P)/S composites with enhanced electrochemical performance of lithium-sulfur battery. *Mater. Res. Bull.* **2022**, *145*, 111529. [CrossRef]
62. Tong, Z.M.; Huang, L.; Guo, J.Y.; Gao, Y.; Zhang, H.J.; Jia, Q.L.; Luo, D.; Lei, W.; Zhang, S.W. Simultaneously achieving fast sulfur redox kinetics and high-loading in lithium–sulfur batteries. *Carbon* **2022**, *187*, 451–461. [CrossRef]
63. Chen, J.S.; Liu, Y.; Liu, Z.K.; Chen, Y.; Zhang, C.G.; Yin, Y.N.; Yang, Q.L.; Shi, Z.Q.; Xiong, C.X. Carbon nanofibril composites with high sulfur loading fabricated from nanocellulose for high-performance lithium-sulfur batteries. *Colloids Surfaces A* **2020**, *603*, 125249. [CrossRef]
64. Li, H.; Liu, D.; Zhu, X.X.; Qu, D.Y.; Xie, Z.Z.; Li, J.S.; Tang, H.L.; Zheng, D.; Qu, D.Y. Integrated 3D electrodes based on metal-nitrogen-doped graphitic ordered mesoporous carbon and carbon paper for high-loading lithium-sulfur batteries. *Nano Energy* **2020**, *73*, 104763. [CrossRef]
65. Zhao, T.Q.; Tan, X.H.; Song, L.T.; Guo, L.M.; Liu, Y.L.; Kang, X.H.; Meng, X.M.; Wang, H.F.; Chu, W.G. Up-Scalable Conversion of White-Waste Polystyrene Foams to Sulfur, Phosphorus-Codoped Porous Carbon for High-Performance Lithium–Sulfur Batteries. *ACS Appl. Energy Mater.* **2020**, *3*, 9369–9378. [CrossRef]
66. Han, H.S.; Wang, T.; Zhang, Y.G.; Nurpeissova, A.; Bakenov, Z. Three-Dimensionally Ordered Macroporous ZnO Framework as Dual-Functional Sulfur Host for High-Efficiency Lithium-Sulfur Batteries. *Nanomaterials* **2020**, *10*, 2267. [CrossRef]